

Ultra-Compact Balanced Multiband Fully Reconfigurable Bandstop Filter

Dubari Borah and Thottam S. Kalkur*

Abstract—This paper introduces a balanced (differential) multiband reconfigurable (tunable) bandstop filter (BSF) using all lumped elements. The main features of the design include its ultra-compact size as well as flexibility to control any frequency band independently in terms of both center frequency and absolute bandwidth (ABW). In the proposed structure, the corresponding non-resonating nodes (NRN) of the symmetrical bisections are connected to N number of LC π -circuits (N-band cell) through capacitors. Again, in each symmetrical bisection, K number of NRNs are series cascaded through LC π -circuits. This results in a Kth order N-band stopband (notch) response in differential mode (DM) operation whereas provides a passband response when excited by a common mode (CM) signal. Reconfiguration of any DM stopband is obtained by using tunable capacitors for the corresponding LC π -circuit in each N-band cell and also, for its coupling capacitors to the NRNs. To validate the proposed topology, a dualband differential tunable BSF is designed and fabricated where both DM stopbands are controlled independently in the range of 1.16 GHz–1.32 GHz. Also, the bandwidth of each band is varied independently by 20–50 MHz without affecting the other band. At any tuning state, DM stopband rejection for each band is found to be ≥ 19 dB, resulting in a minimum CMRR value of 19 dB. The fabricated prototype occupies an area of $0.13\lambda_g \times 0.04\lambda_g$ (21 mm \times 7 mm) where λ_g is the guided wavelength at the center frequency of the entire spectral range, and the experimental results show a good agreement with the simulation results.

1. INTRODUCTION

Due to relatively high immunity to environmental noise, the popularity of balanced circuit is increasing day by day. In any RF and microwave system, bandstop filter (BSF) plays a vital role for protecting the required signals from outside interference and therefore, it should be also implemented in differential topology. Moreover, modern communication systems with multiband services require BSFs with multiple stopbands [1, 2]. For example, dualband BSFs are often used in high power amplifiers and mixers due to their capability of rejecting double sideband spectrum [3, 4]. Similarly, a multiband differential BSF with high CMRR, high stopband attenuation, high selectivity, and ultra-compact physical size will have great demand in UHF band applications as many RF systems operate in that range.

Moreover, the reconfigurable circuitry is getting much attention recently in electronic industry, whether it is a digital application such as embedded system, data mining etc. [5, 6] or it is an RF front-end application such as amplifier, antenna etc. [7, 8]. To meet the quickly and continuously evolving wireless standards, adaptive circuits help designers to avoid overdesigning or full replacement of the existing outdated hardware. Therefore, it is important to incorporate reconfiguration with multiband differential BSF. So far, tunability has been discussed for differential BSF with single frequency band

Received 14 January 2020, Accepted 5 March 2020, Scheduled 10 March 2020

* Corresponding author: Thottam S. Kalkur (tkalkur@uccs.edu).

The authors are with the Microelectronics Research Laboratory, Department of Electrical and Computer Engineering, University of Colorado, Colorado Springs, CO 80918-7150, USA.

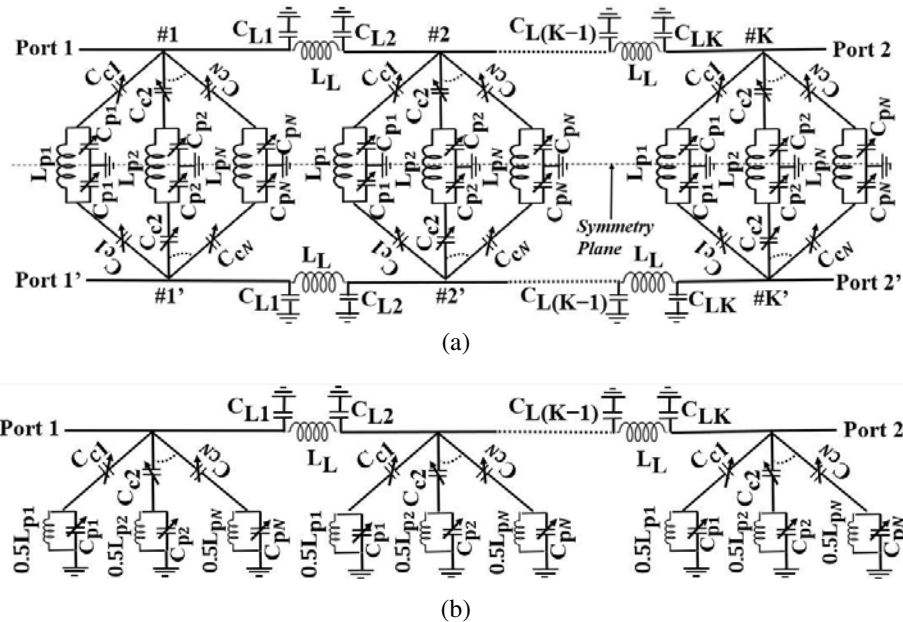
response in [9, 10]. However, these two designs are very complex due to the employment of substrate integrated waveguide resonators and double-sided parallel-strip line, respectively. Also, the CM insertion loss associated with the design in [10] is very high which limits the possibility of obtaining the optimum CMRR with it. In [11], a multiband differential BSF is presented, but it is not tunable. The multiband balanced BSF design in [12] is reconfigurable, but its size is significantly large for UHF band applications, and the realizable fractional bandwidth is limited due to the use of distributed elements. Another shortcoming associated with both the designs in [11] and [12] is that they require open stubs along the symmetry plane to achieve high CMRR.

This paper introduces a differential reconfigurable multiband BSF with all lumped elements for the first time based on the microstrip differential BSF design reported in [12]. The design is symmetrical about the horizontal central plane. Each symmetrical bisection is comprised of K number of N -band filtering cells, series cascaded through LC π -circuits to achieve a K -th order N -band BSF response in differential mode (DM) whereas CM signal is simply bypassed by the circuit due to its inherent balanced property. The structure benefits from the independent control of any frequency band, in terms of both center frequency and absolute bandwidth. Moreover, due to the symmetrical property of balanced structure, the design provides a high CMRR, and there is no need of loading the symmetry plane with any additional component.

The manuscript is organized as follows. Section 2 gives a detailed description of the design and the theory behind it. In Section 3, an example of dualband tunable differential filter is presented to describe the design methodology. Section 4 provides the measured results from the fabricated prototype to compare with the simulation results. Section 5 summarizes the main points of this research as conclusion.

2. PROPOSED TOPOLOGY

Figure 1 shows the proposed multiband reconfigurable balanced BSF with all lumped elements. This four-port design is symmetrical about the horizontal central plane and each symmetrical bisection has K nodes; series cascaded through LC π -circuits. Each node in one symmetrical bisection shares N number of LC π -sections (L_{pi}, C_{pi}) with the corresponding node in the other bisection. In DM operation, the central plane acts as a perfect electric wall or electric short-circuit (Figure 1(b)). Therefore, the DM equivalent circuit produces a K th order N -band BSF response (Figure 1(d)) where any frequency band can be tuned by simply employing variable capacitors for the corresponding C_{pi} and its coupling capacitor C_{ci} in each N -band filtering cell, respectively. On the other hand, the symmetry plane in CM operation behaves like a perfect magnetic wall or electric open circuit (Figure 1(c)). As a result, it



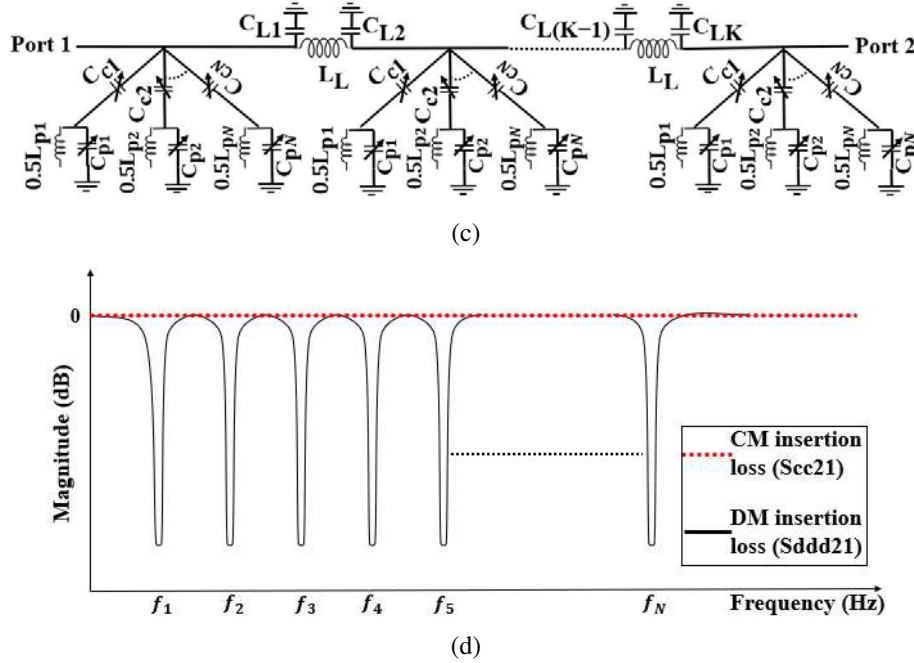


Figure 1. (a) Proposed balanced multiband reconfigurable BSF. (b) DM equivalent circuit. (c) CM equivalent circuit. (d) DM insertion loss (Sddd21) and CM insertion loss (Scc21) at any tuning state.

cannot produce those N stopbands, rather produces a passband response due to its inherent symmetrical property (Figure 1(d)).

The extraction of all elements in Figure 1(a) will be discussed in the following section, starting with an example of reconfigurable dualband balanced BSF.

3. DESIGN EXAMPLE

The design process starts with the extraction of DM equivalent circuit. At any tuning state, the DM multiband frequency transformation associated with this topology is given by [12],

$$\Omega_{MBBSF}(f) = - \sum_{i=1}^N \frac{1}{\Delta_i \left(\frac{f}{f_i} - \frac{f_i}{f} \right)} \tag{1}$$

where Ω is the normalized lowpass frequency; N is the total number of stopbands; f is the frequency variable; f_i and Δ_i are the center frequency and bandwidth scaling factor of the i th stopband, respectively.

To illustrate in detail, an example of balanced dualband tunable BSF is considered here. Applying Eq. (1), a standard two pole Chebyshev lowpass ladder network with shunt capacitances is transformed into the DM equivalent circuit, which is a second order dualband BSF. It is shown in Figure 2(a) where Res1 and Res2 are quarter-wavelength lines at resonant frequencies f_1 and f_2 , respectively and J_{s1} , J_{s2} , J_{12} are the immittance inverters. These inverter-coupled quarter-wavelength resonators are equivalent to series LC resonators. Therefore, equating the input impedances at resonance, the relationships among different parameters are shown below, where $g_0 - g_3$ are the element values of the lowpass filter prototype [13–15].

$$J_{12} = \frac{Z_0}{\sqrt{g_0 \cdot g_3}} \tag{2}$$

$$Z_{res1} = \frac{\sqrt{\pi \Delta_1 g_1}}{2J_{s1}} \tag{3}$$

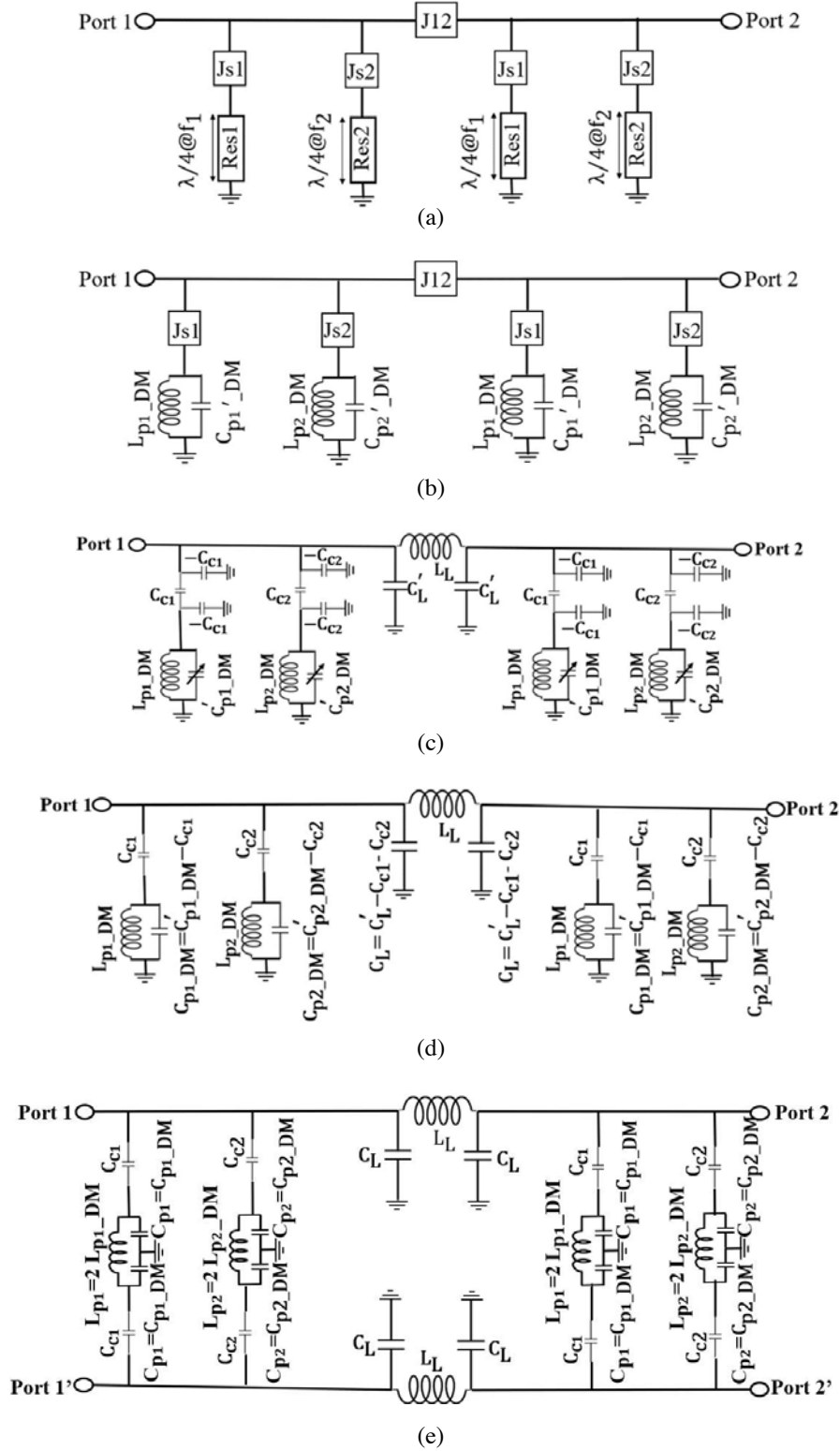


Figure 2. Derivation of the differential dualband BSF circuit. (a) Dualband filter section using $\lambda/4$ resonators and scaling inverters. (b) Transformation of $\lambda/4$ resonators to LC parallel resonators. (c) Representation of all inverters as lumped element π -circuits. (d) DM equivalent circuit. (e) Overall differential circuit realization using inductors and capacitors.

$$Z_{res2} = \frac{\sqrt{\pi\Delta_2g_1}}{2J_{s2}} \quad (4)$$

In Figure 2(b), Res1 and Res2 are replaced by their equivalent LC parallel resonators. The equations for calculating the elements of these parallel resonant circuits are [16]

$$L_{p1_DM} = \frac{\Delta_1g_1}{\omega_1 Z_{res1} J_{s1}^2} \quad (5)$$

$$C'_{p1_DM} = \frac{Z_{res1} J_{s1}^2}{\omega_1 \Delta_1g_1} \quad (6)$$

$$L_{p2_DM} = \frac{\Delta_2g_1}{\omega_2 Z_{res2} J_{s2}^2} \quad (7)$$

$$C'_{p2_DM} = \frac{Z_{res2} J_{s2}^2}{\omega_2 \Delta_2g_1} \quad (8)$$

In Figure 2(c), J_{12} , J_{s1} , and J_{s2} are replaced by their equivalent lumped element π -circuits, and Equations (9)–(13) are used to calculate them [13, 16, 17]. Usually, to achieve good selectivity in DM operation, L_L and C'_L values should be calculated for $J_{12} = 50 \Omega$ [13].

$$L_L = J_{12}/\omega_0 \quad (9)$$

$$C'_L = 1/(J_{12} \cdot \omega_0) \quad (10)$$

$$C_{c1} = J_{s1}/\omega_1 \quad (11)$$

$$C_{c2} = J_{s2}/\omega_2 \quad (12)$$

$$\omega_0 = (\omega_1 + \omega_2)/2 \quad (13)$$

The negative capacitors will be absorbed into C'_L , C'_{p1_DM} and C'_{p2_DM} to give the DM equivalent circuit in Figure 2(d). By setting L_{p1_DM} (or C_{p1_DM}) and L_{p2_DM} (or C_{p2_DM}) to any physically realizable values, scaling inverters J_{s1} and J_{s2} are obtained. Similarly, L_L and C'_L are calculated for $Z_0 = 50 \Omega$. Therefore, the closed form equations of all the elements in Figure 2(d) are

$$C_{c1} = \sqrt{\frac{\Delta_1g_1}{L_{p1_DM} Z_{res1} \omega_1^3}} \quad (14)$$

$$C_{p1_DM} = \frac{1}{\omega_1^2 L_{p1_DM}} - C_{c1} \quad (15)$$

$$C_{c2} = \sqrt{\frac{\Delta_2g_1}{L_{p2_DM} Z_{res2} \omega_2^3}} \quad (16)$$

$$C_{p2_DM} = \frac{1}{\omega_2^2 L_{p2_DM}} - C_{c2} \quad (17)$$

$$L_L = \frac{Z_0}{\omega_0 \sqrt{g_0g_3}} \quad (18)$$

$$C_L = \frac{\sqrt{g_0g_3}}{Z_0\omega_0} - C_{c1} - C_{c2} \quad (19)$$

The ideal differential dualband circuit is obtained by repeating and folding the DM equivalent circuit. It is depicted in Figure 2(e) where $L_{p1} = 2L_{p1_DM}$, $L_{p2} = 2L_{p2_DM}$, $C_{p1} = C_{p1_DM}$ and $C_{p2} = C_{p2_DM}$.

For a dualband differential filter with DM specifications — $f_1 = 1.15$ GHz, $f_2 = 1.31$ GHz and $\Delta_1 = \Delta_2 = 3\%$, the transmission line model is shown in Figure 3(a), and using Equations (14)–(19), initial optimization parameters of the equivalent lumped element circuit are shown in Figure 3(b). Figure 4(a) compares the simulation results of these two models which demonstrate that the rejection of each differential stopband for the lumped element design ($Q = 200$) is about 10 dB less than its equivalent microstrip design (using Rogers RO4003). For the microstrip design, the rejection at any

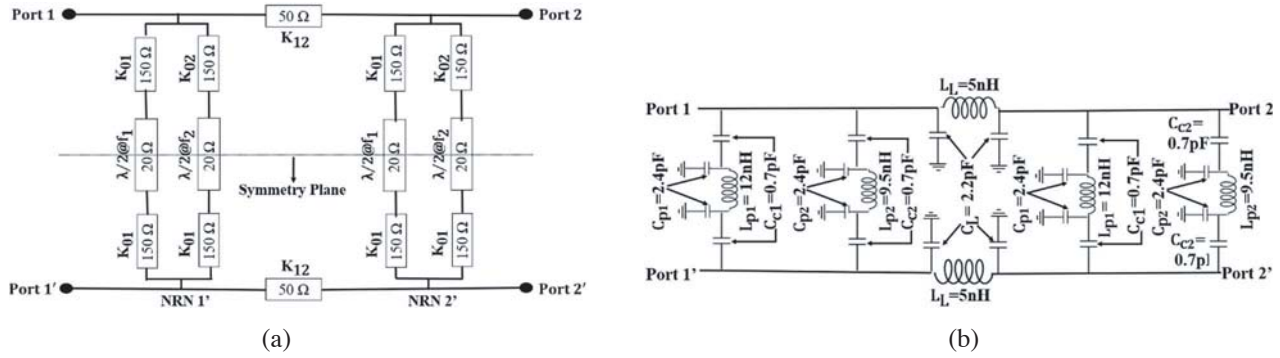
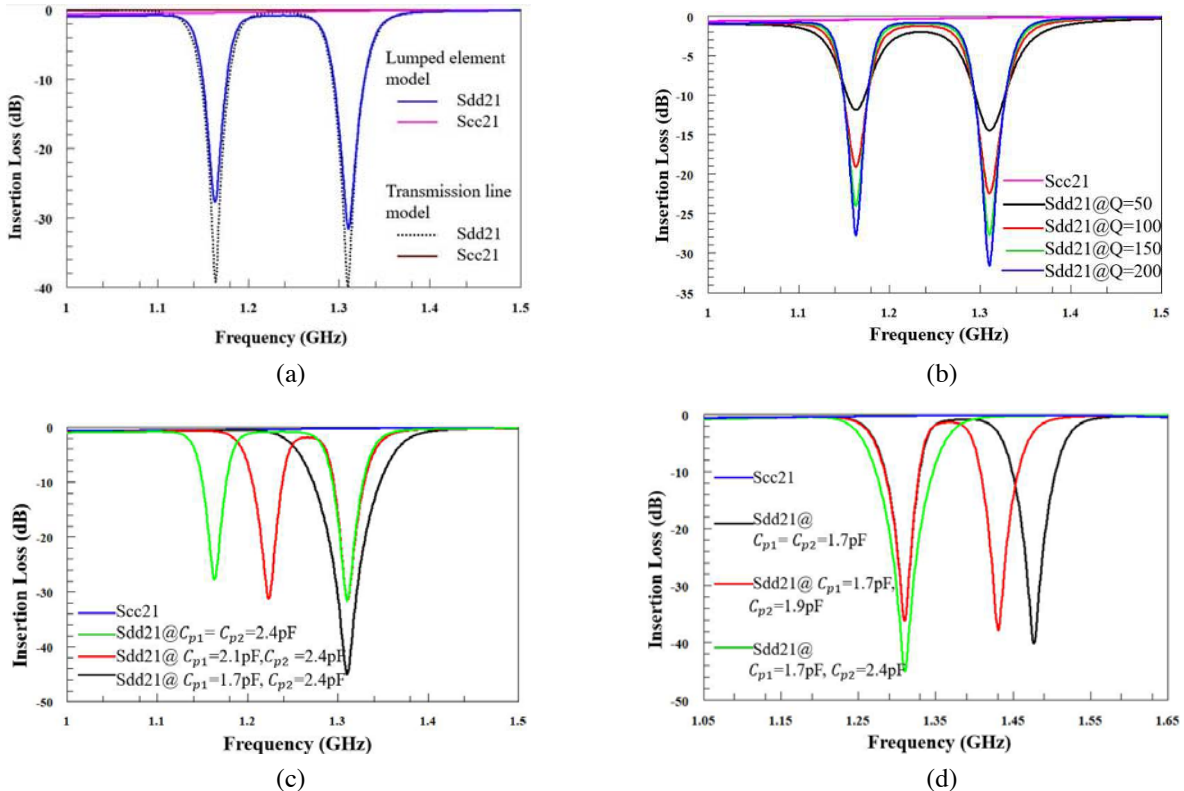


Figure 3. (a) Transmission line model and (b) equivalent lumped element model of the differential dualband BSF design with the given specifications.

resonant frequency is mainly determined by the dielectric loss of the substrate whereas for the LC circuit, it is mainly determined by the component Q. To optimize the output, high-Q elements should be used for building the entire filter, especially for the L_{p1} , L_{p2} , C_{p1} and C_{p2} . Figure 4(b) shows that as the resonator Q in DM equivalent circuit changes from 50 to 200, the lower band rejection improves from 12 dB to 28 dB whereas the upper band rejection lies in the range of 14.5 dB–31.6 dB. From the above equations, by varying the values of C_{c1} ; C_{p1} or C_{c2} ; C_{p2} , both center frequencies and bandwidths of the DM stopbands can be controlled. Keeping C_{c1} and C_{c2} values constant, Figures 4(c) and (d) illustrate the independent tuning of each band within the range of 1.16 GHz–1.31 GHz. It should be noted that within the frequency agile range of each band, its ABW is also varying. This is because only C_{p1} or C_{p2} is changed to tune the center frequency but corresponding coupling (C_{c1} or C_{c2}) has not been changed. The bandwidth of each band is mainly controlled by the coupling capacitor. Also, when the both bands merge, the bandwidth gets wider without any increase in the order of the filter response.



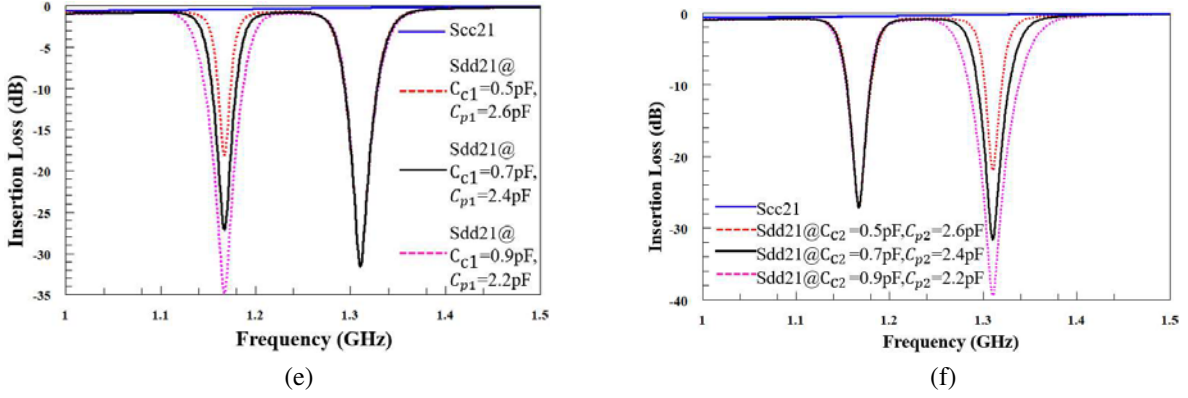


Figure 4. Various Frequency responses. (a) Comparison of results from EM simulation of the microstrip model and circuit simulation of the lumped element design in Figure 3(b). Effect of component Q in the lumped element design. (c) Independent center frequency tuning of lower stopband using the lumped element design. (d) Independent center frequency tuning of upper stopband using the lumped element design. (e) Bandwidth control of lower band using the lumped element design. (f) Bandwidth control of upper band using the lumped element design.

This is because the two resonators in each dualband section are connected in parallel without sharing any equivalent impedance inverter between them. Figures 4(e) and (f) demonstrate the independent bandwidth control of each frequency band, keeping the center frequency constant. It is achieved by varying $C_{c1}; C_{p1}$ or $C_{c2}; C_{p2}$, respectively. The bandwidth of the lower band changes from 34 MHz to 62 MHz whereas the upper stopband bandwidth changes in the range of 43 MHz–82 MHz.

Now, Equations (14)–(19) can be generalized for extracting the components of the multiband differential BSF structure in Figure 1(a) as follows, where $i = \{1, 2, \dots, N\}$ and $j = \{1, 2, \dots, K\}$.

$$L_L = \frac{Z_0}{\omega_0 \sqrt{909K+1}} \quad (20)$$

$$C_{ci} = \begin{cases} \sqrt{\frac{\Delta_i g_i}{0.5 L_{pi} Z_{resi} \omega_i^3}} & \text{if } i \text{ is odd} \\ \sqrt{\frac{\Delta_i g_i g_{K+1}}{0.5 L_{pi} Z_{resi} \omega_i^3}} & \text{if } i \text{ is even} \end{cases} \quad (21)$$

$$C_{pi} = \frac{1}{0.5 L_{pi} \omega_i^2} - C_{ci} \quad (22)$$

$$C_{Lj} = \begin{cases} \frac{\sqrt{909K+1}}{Z_0 \omega_0} - \sum_{i=1}^N C_{ci} & \text{if } j = 1, K \\ 2 \frac{\sqrt{909K+1}}{Z_0 \omega_0} - \sum_{i=1}^N C_{ci} & \text{if } j \neq 1, K \end{cases} \quad (23)$$

4. RESULTS AND DISCUSSION

To verify the proposed topology, a prototype of the above-mentioned dualband tunable differential BSF is fabricated on a Rogers RO4003 substrate with dielectric constant 3.38, substrate thickness 1.52 mm, and loss tangent 0.0027 @1 GHz (Figure 5 and Table 1). The implemented circuit uses 0402 series wirewound inductors ($Q > 55$ @1 GHz) and 0805 S-series multi-layer, high- Q capacitors ($Q > 900$ @1 GHz) from Johanson Technology as well as Skyworks SMV1231 series varactors for tunable response.

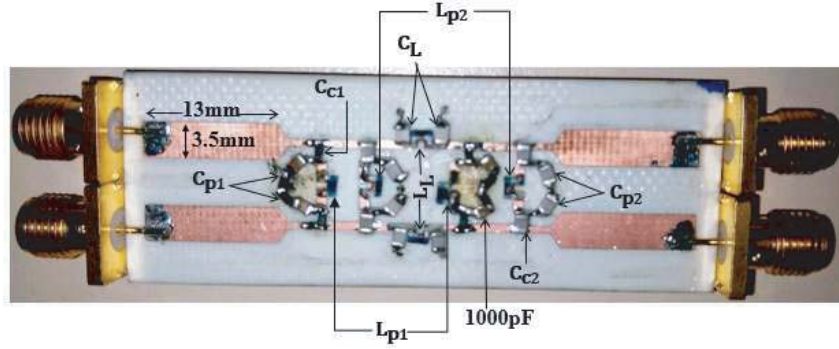


Figure 5. Fabricated prototype of the differential dualband tunable BSF.

DC blocking capacitors of 1000 pF are also used in the circuit. The design layout is optimized and simulated in NI/AWR microwave office and the prototype is characterized with the help of N5224 4-port PNA. Satisfactory agreement has been found between the simulated and measured results. Figure 6(a) illustrates that with $C_{p1} = C_{p2} = 2.4$ pF, the design exhibits dualband BSF response in DM operation with center frequencies 1.16 GHz and 1.31 GHz, respectively. The stopband rejection for both bands (Sdd21) is ≥ 19 dB whereas Scc21 plot is a flat 0 dB passband response. The FBWs of the both DM stopbands are close to 3%. The DM return loss (Sdd11) for each band is found to be ≤ 1 dB (Figure 6(b)). As the Sdd21 mainly depends upon the component Q, it can be improved by using high-Q components for the circuit. It will also help getting a better in-band Sdd11 value for each differential band. Figure 6(c) shows the independent control of the lower DM stopband. It tunes in the range of 1.16 GHz–1.31 GHz while its Sdd21 value varies from about 20 dB to 38 dB. Also, its ABW of 37 MHz at 1.16 GHz has changed to 100 MHz at 1.31 GHz due to the merging with the upper stopband. Some variation between the simulated response and the measured response is obvious due to the slight difference in the component values as well as effect of parasitic in the built prototype. In Figure 6(d), the ABW of the lower band is tuned from 37 MHz to 90 MHz, keeping the center frequency constant

Table 1. Component values for the prototype in Figure 5.

Elements	L_{p1}	C_{p1}^*	C_{c1}^*	L_{p2}	C_{p2}^*	C_{c2}^*	L_L	C_L
Value	12 nH	2.4 pF	0.7 pF	10 nH	2.4 pF	0.7 pF	5.1 nH	2 pF

C_{p1} , C_{c1} , C_{p2} and C_{c2} values vary for different results demonstrated below.

Table 2. Comparison with state-of-the-art balanced BSFs.

Parameters	[9]	[10]	[12]	[18]	[19]	This Work
# of Stopbands	1	1	2(*)	1	1	2(*)
Center frequency Control	Yes	Yes	Yes	–	–	Yes
Bandwidth Control	–	–	–	–	–	Yes
Minimum Sdd21 (dB)	47	10.5	26/21	15	18.89	19/21
Maximum Sdd11 (dB)	0.5	8	4(*)	–	2.5	2.3
Scc21 (dB) in 3 dB DM bandwidths	0	13	0	0	50.45	0
Minimum CMRR (dB)	47	2.5	26/21	15	31.56	19/21
Effective size in $\lambda_g \times \lambda_g$ (mm \times mm) *	$0.26\lambda_g \times 0.24\lambda_g$ (44 mm \times 40 mm)	$0.21\lambda_g \times 0.21\lambda_g$ (95 mm \times 95 mm)	$1.27\lambda_g \times 0.61\lambda_g$ (160 mm \times 77 mm)	–	$0.58\lambda_g \times 0.3\lambda_g$ (52 mm \times 26.75 mm)	$0.13\lambda_g \times 0.04\lambda_g$ (21 mm \times 7 mm)

of stopbands can be extrapolated to an arbitrary number and λ_g denotes the guided wavelength at center frequency of all DM stopbands.

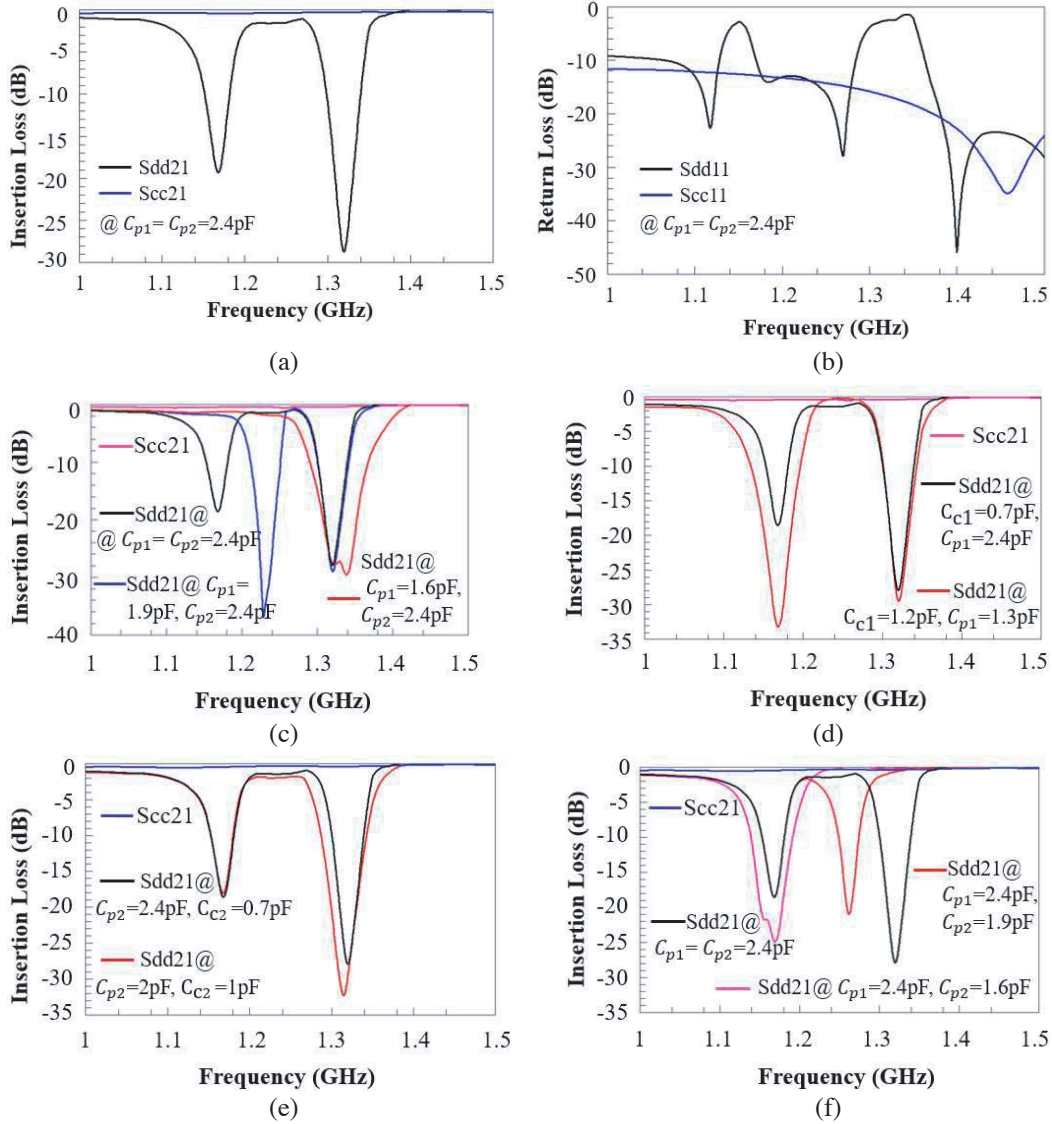


Figure 6. Example differential dualband response with (a) insertion loss and (b) return loss at $C_{p1} = C_{p2} = 2.4$ pF. (c) Independent control of lower band center frequency. (d) Bandwidth control of lower band. (e) Bandwidth control of upper band. (f) Independent control of upper band center frequency.

at 1.16 GHz. Similarly, Figure 6(e) demonstrates the bandwidth control of the upper stopband from 47 MHz to 74 MHz at center frequency 1.31 GHz. In Figure 6(f), the frequency agility of the upper band is illustrated. As it shifts towards lower frequency, its ABW of 47 MHz at 1.31 GHz is continuously varying and finally results in a wider bandwidth of 82 MHz while merging with the lower band at 1.16 GHz. At any tuning state, the DM insertion loss for this upper band is found to be > 21 dB.

Finally, Table 2 shows the comparison between the fabricated model using the proposed topology and already published related work. Its main advantage over the listed designs lies on the fact that it is one of those two designs which can incorporate arbitrary number of stopbands, and most importantly, all the bands can be reconfigured independently, in terms of both center frequency and bandwidth. Also, it provides a reasonable CMRR value for all tuning states whereas DM return loss is better than all other designs except [9]. Finally, the novelty or the most significant attribute of this design is shown in the last row of the table. It demonstrates that the space occupied by this design is much smaller than the other designs.

5. CONCLUSION

A fully reconfigurable multiband balanced BSF with all lumped elements is presented for the first time in this paper. Each symmetrical bisection of the four-port balanced structure is designed by cascading multiband cells in series through LC π -networks. For DM operation, each multiband cell can be considered as N LC parallel circuits, coupled to the same node through N capacitors. Therefore, K series cascaded N-band cells produce a K th order N-band DM response. Reconfiguration of any band is achieved by using variable capacitors for the corresponding LC parallel circuit as well as for its coupling capacitor in each filtering cell. As the LC resonators corresponding to different bands are connected in parallel to each other in each multiband cell, it provides flexibility to control both center frequency and bandwidth of any band independently, without affecting the others. The CM noise at any tuning state is highly eliminated due to the inherent symmetrical property of the balanced structure. To illustrate the proposed topology, a lumped element prototype of second order balanced dualband tunable BSF is designed and fabricated. The tunability of each band is shown in the range of 1.16 GHz–1.31 GHz whereas a bandwidth control of 20 to 50 MHz is also discussed. At any tuning state, it maintains a CMRR value of better than 19 dB for each band. The fabricated prototype occupies an area of $0.003\lambda_g^2$ and the experimental results show a good agreement with the simulation results.

REFERENCES

1. Khokle, R., R. Kumar, R. V. S. Ram Krishna, and N. Kushwaha, "Design and analysis of multi-band filters using slot loaded stepped impedance resonators," *Progress In Electromagnetics Research B*, Vol. 56, 137–160, 2013.
2. Kamma, A., S. R. Gupta, G. S. Reddy, and J. Mukherjee, "Multi-band notch uwb band pass filter with novel contiguous split rings embedded in symmetrically tapered elliptic rings," *Progress In Electromagnetics Research C*, Vol. 39, 133–148, 2013.
3. Chen, F., J. Qiu, and Q. Chu, "Dual-band bandstop filter using stub-loaded resonators with sharp rejection characteristic," *Electronics Letters*, Vol. 49, No. 5, 351–353, February 28, 2013.
4. Wang, W., M. Liao, Y. Wu, and Y. Liu, "Small-size high-selectivity bandstop filter with coupled-line stubs for dual-band applications," *Electronics Letters*, Vol. 50, No. 4, 286–288, February 13, 2014.
5. Shahrouzi, S. N., "Optimized embedded and reconfigurable hardware architectures and techniques for data mining applications on mobile devices," Ph.D. Dissertation, University of Colorado Colorado Springs, December 2018.
6. Shahrouzi, S. N. and D. G. Perera, "Dynamic partial reconfigurable hardware architecture for principal component analysis on mobile and embedded devices," *EURASIP Journal on Embedded Systems*, Vol. 2017, Article No. 25, Springer Open, February 2017.
7. Xie, J.-J. and Q. Song, "Wideband dual-polarized dipole antenna with differential feeds," *Progress In Electromagnetics Research Letters*, Vol. 59, 43–49, 2016.
8. Yang, J.-R., H.-C. Son, and Y.-J. Park, "A class E power amplifier with coupling coils for a wireless power transfer system," *Progress In Electromagnetics Research C*, Vol. 35, 13–22, 2013.
9. Hagag, M. F., M. Abdelfattah, and D. Peroulis, "Balanced octave-tunable absorptive bandstop filter," *2018 IEEE 19th Wireless and Microwave Technology Conference (WAMICON)*, 1–4, Sand Key, FL, 2018.
10. Cai, J., Y. J. Yang, W. Qin, and J. X. Chen, "Wideband tunable differential bandstop filter based on double-sided parallel-strip line," *IEEE Transactions on Components, Packaging and Manufacturing Technology*, Vol. 8, No. 10, 1815–1822, 2018.
11. Borah, D. and T. S. Kalkur, "A planar multiband balanced bandstop filter," *2018 IEEE MTT-S Latin America Microwave Conference (LAMC 2018)*, 1–3, Arequipa, Peru, 2018.
12. Borah, D. and T. S. Kalkur, "Tunable multiband balanced bandstop filter with high CMRR," *Progress In Electromagnetics Research C*, Vol. 97, 1–13, 2019.
13. Hunter, I. C., *Theory and Design of Microwave Filters*, IEE Press, London, U.K., 2001.

14. Pozar, D. M., *Microwave Engineering*, Wiley, Hoboken, NJ, 2012.
15. Hong, J.-S., *Microstrip Filters for RF/Microwave Applications*, Wiley, Hoboken, NJ, 2011.
16. Ou, Y. and G. M. Rebeiz, "Lumped-element fully tunable bandstop filters for cognitive radio applications," *IEEE Transactions on Microwave Theory and Techniques*, Vol. 59, No. 10, 2461–2468, October 2011.
17. Elsbury, M. M., P. D. Dresselhaus, S. P. Benz, and Z. Popovic, "Integrated broadband lumped-element symmetrical-hybrid N-way power dividers," *2009 IEEE MTT-S International Microwave Symposium Digest*, 997–1000, Boston, MA, 2009.
18. Sorocki, J., I. Piekarz, S. Gruszczynski, and K. Wincza, "Low-loss directional filters based on differential band-reject filters with improved isolation using phase inverter," *IEEE Microwave and Wireless Components Letters*, Vol. 28, No. 4, 314–316, April 2018.
19. Kong, M., Y. Wu, Z. Zhuang, and Y. Liu, "Narrowband balanced absorptive bandstop filter integrated with wideband bandpass response," *Electronics Letters*, Vol. 54, No. 4, 225–227, February 27, 2018.